

Particle size manipulation as an influential parameter in the development of mechanical properties in electric arc furnace slag-based AAM



Katja Traven^a, Mark Češnovar^{a,b}, Vilma Ducman^{a,*}

^a Slovenian National Building and Civil Engineering Institute, Dimičeva 12, 1000, Ljubljana, Slovenia

^b Jozef Stefan International Postgraduate School, Jamova Cesta 39, 1000, Ljubljana, Slovenia

ARTICLE INFO

Keywords:

Alkali-activated materials (AAM)
Electric arc furnace steel slag
Mechanical activation
Mechanical properties
Porosity

ABSTRACT

Alkali-activated materials (AAM) have gained recognition as a promising alternative to technical ceramic and building materials owing to the lower energy demands for production and the potential to use slag as a precursor. In the present study, five sets of slag-based AAM pastes were prepared with different particle sizes (fractions $d < 63$, $63 < d < 90$, and $90 < d < 125 \mu\text{m}$ in different mass ratios) under the same curing regime and using a fixed precursor to activator (water) mass ratio. Precursors and the hardened AAM are evaluated using BET, XRD, XRF, SEM, FTIR, reactivity of precursors by leaching, and mercury intrusion porosimetry (MIP). Chemical analysis indicated only marginal differences among the different-sized fractions of input materials, whereas the BET surface area and reactivity among the precursors differed significantly—smaller particles had the largest surface area, and thus, higher reactivity. The mineralogical differences between the precursors and hardened AAM were negligible. The results revealed that compressive strength was significantly influenced by particle size, i.e., a threefold increase in strength when the particle size was halved. Microstructural evaluation using MIP confirmed that the porosity was the lowest in AAM with the smallest particle size. The low porosity and high reactivity of the fine fractions led to the highest compressive strength, confirming that manipulation of particle size can significantly influence the mechanical properties.

1. Introduction

Ordinary Portland cement (OPC) production contributes significantly to global CO₂ emissions. The latest estimates suggest that it accounts for approximately 8% of the total anthropogenic release of CO₂ (an estimated value of $1.45 \pm 0.20 \text{ Gt}$) [1], which explains the recent interest in identifying alternative construction materials and binders. Alkali-activated materials (AAM), also called geopolymers or inorganic polymers, are recognized as promising alternatives to building materials and ceramics owing to the lower energy demand for their production. Furthermore, they can be produced using inorganic wastes or industrial residues, reducing the disposal of waste materials in landfills. AAM are inorganic systems containing a solid component called a precursor, which consists of reactive Al₂O₃ and SiO₂ (in its semi-crystalline to amorphous phases), and an alkali-activating solution called an activator, which consists primarily of alkali metal-based silicates and/or hydroxides [2]. Numerous kinds of source materials are suitable for use as a precursor, including metakaolin [3], kaolin [4], fly ash (FA) [5], volcanic ash [6], and different slags [7]. Because of the diversity in possible precursors, AAM can be designed to include the

finest properties compared to the conventionally used binders, such as improved heat resistance [8], reduced drying shrinkage and creep [9], superior resistance to acids and sulphates [10,11], and higher strength [12]. AAM can therefore serve as an alternative or supplementary binder, depending on the local availability of raw materials [13]; e.g., in the Ukraine their use is today included in legislation [14].

Slags, which are currently underutilized partially crystalline metallurgical residues, are the by-products of steelmaking processes where the metallic and non-metallic constituents are separated from raw ore. Several kinds of slag obtained from the different processes of steelmaking are already used as precursors in AAM, including blast furnace slag (air-cooled (ABFS) [15] or granulated (GBFS) [16]), basic oxygen furnace slag (BOS) [17], electric arc furnace slag (EAF) [18–20], secondary metallurgical slag (e.g., ladle furnace slag [21]) and others (e.g., desulphurization slag [22]). EAF slag is produced by an electric arc furnace in the primary refining stage during the manufacture of crude steel. In this process, an electric current is used to heat the lime and/or dolomite fluxes to a liquid state. Throughout the melting procedure, the fluxes are combined with steel-incompatible parts and non-metallic scrap constituents to form a liquid slag, which floats on the top of the

* Corresponding author.

E-mail address: vilma.ducman@gmail.com (V. Ducman).

<https://doi.org/10.1016/j.ceramint.2019.07.296>

Received 16 April 2019; Received in revised form 24 July 2019; Accepted 25 July 2019

Available online 26 July 2019

0272-8842/ © 2019 The Authors. Published by Elsevier Ltd. This is an open access article under the CC BY-NC-ND license

(<http://creativecommons.org/licenses/by-nc-nd/4.0/>).

molten steel and is then separated and cooled, forming crystalline slag. The chemical composition of slag differs according to the type of metallurgical treatment, conditions, and the additives used during the manufacturing process [23]. In Europe, the average production of EAF slag is approximately 6 Mt/year, of which 13% is destined for landfills and a further 11% is held in interim storage, which presents a significant possibility for its utilization [23].

The mechanical and chemical properties of AAM are strongly dependent on numerous factors including the type and amount of precursor used, presence of an amorphous phase, type of activator used, curing regime, and particle size of the precursor [24–28]. For example, Wang et al. investigated GBFS activated by water glass at different curing temperatures and activator concentrations [29]. Burciaga-Diaz et al. explored the influence of the silicate modulus on the change in microstructure [30]. They determined that the compressive strength achieved was 90 MPa, after 28 days of curing at room temperature, when the silicate modulus was in the range of 1–1.5. In another study, Gebregziabihier et al. exposed alkali-activated GBFS samples to heat curing and investigated the mechanism and microstructure of the alkali-activation process [31]. Recently, Ozturk et al. reported an extensive study on the activation of EAF slag while varying the silicate modulus (SM), sodium concentrations (SC), relative humidity (RH), curing temperatures (CTemp), and curing times (CTime) [32]. The best performance of the mortar specimen (compressive and flexural strengths of 22.0 and 4.2 MPa, respectively) was achieved when SM, SC, RH, CTemp, and CTime were 2, 6%, 98%, 80 °C, and 12 h, respectively.

Different approaches in precursor pretreatment have been adopted, which aim to improve the mechanical properties of the hardened AAM. These include mechanical activation via ball milling [33], electromagnetic vortex milling [34], and thermal activation [4,35]. Traditional mechanical activation is typically achieved by high-energy milling machinery. Changes caused in the material throughout the milling process include particle size reduction, increase in specific surface area, morphological changes, structural defects, and an increase in the degree of amorphous phase and implied structural rearrangement. The most vital consequence of the transformation occurring in the material during mechanical activation is an increased reactivity and thus improved mechanical properties. Marjanović et al. conducted mechanical activation using a planetary ball mill and after only 15 min the size of the FA reduced dramatically (10-fold, with a significant amount of FA micro particles transforming into nanoparticles), resulting in an increase in compressive strength from 11 up to 35-times compared to the AAM samples without mechanical activation [33]. Hounsi et al. also investigated the influence of the mechanical activation of raw kaolin by dry ball-milling, and found a 35% higher compressive strength of AAM cured for 72 h at 70 °C than those without activation [36]. Furlani et al. studied the production and characterization of geopolymers prepared by mixing steel slag of two different sizes (under 125 and 250 μm) and metakaolin where the composition containing 40 wt % of steel slag (with particle size under 125 μm) and 60 wt % of metakaolin exhibited the highest compressive strength [37]. In a short communication, Al Bakri et al. reported an increase in compressive strength with a decrease in particle size of blast furnace slag [12]. However, there is a lack of comprehensive studies that systematically investigate particle size as an influential parameter in the alkali-activation process of slag. Therefore, to the best of the authors' knowledge, this is the first study to systematically investigate this aspect in slag-based AAM.

This study develops on our previously published paper where curing time and temperature were considered to be influential parameter in slag-based alkali-activating processes [38]. The objective of this study is to evaluate the influence of slag particle size (after mechanical activation) on the mechanical properties (bending and compressive strength) of AAM. Five sets of AAM pastes are prepared using different particle sizes (fractions $d < 63$, $63 < d < 90$, $90 < d < 125$ μm in different mass ratios), while maintaining the same curing regime and a fixed precursor, activator and water mass ratio. First, the mechanical

Table 1
Particle size distribution and BET specific surface area of different-sized slag fractions.

| Precursor | C10 [μm] | C50 [μm] | C90 [μm] | Surface area – BET [m ² /g] |
|------------------------------|----------|----------|----------|--|
| d < 63 μm | 1.38 | 14.96 | 45.02 | 7.61 |
| 63 < d < 90 μm | 1.06 | 16.98 | 57.73 | 6.32 |
| 90 < d < 125 μm | 1.13 | 23.97 | 97.06 | 5.37 |

properties of the AAM samples are evaluated. Then, a microstructural evaluation is performed using mercury intrusion porosimetry (MIP), X-ray powder diffraction (XRD), Fourier-transform infrared (FTIR) spectroscopy, and scanning electron microscopy (SEM).

2. Experimental

2.1. Materials

EAF slag from the metallurgical industry in Slovenia was used for the preparation of the slag-based AAM under investigation. Fractions of three different particle sizes ($d < 63$, $63 < d < 90$, and $90 < d < 125$ μm) were realized through the processes of milling and sieving, each exhibiting different particle size distribution and BET specific surface area (7.61, 6.32, and 5.37 cm²/g, respectively; see Table 1). The chemical compositions of the different-sized fractions of slag under investigation are listed in Table 2. Water glass (potassium silicate Betol K 5020 T; Woellner Austria GmbH; SiO₂:K₂O = 1.63 mass %; 51.5 mass % aqueous solution) was used as the activating solution.

2.2. Preparation of the AAM

AAM designations and compositions prepared for this study (i.e., the selected samples) are presented in Table 3. Five sets of AAM paste were prepared under the same curing regime and using a fixed precursor, activator, and water to mass ratio (except in the case of the 1AKS90 mixture, where a greater amount of water was added owing to the inadequate viscosity of the paste), and then evaluated by particle size (fractions $d < 63$, $63 < d < 90$, $90 < d < 125$ μm in different mass ratios). A designation was formulated as follows: in the first part, 1AKS is the same for all specimens and indicates 1 – number of batch, A – slag A, and KS – potassium silicate. In the second part, the two numbers at the end, e.g., 63–90, indicate the size fraction used; a designation with one number, e.g., 63, indicates the maximum particle size with one or more fractions used. The investigated AAM were synthesized by mixing potassium water glass with a selected fraction of slag, and then adding

Table 2
Chemical composition of different-sized slag fractions used for preparation of AAM (in wt. %).

| | d < 63 μm | 63 < d < 90 μm | 90 < d < 125 μm |
|--------------------------------|-----------|----------------|-----------------|
| LOI 950 °C | 15.47 | 13.46 | 10.98 |
| Na ₂ O | 0.28 | 0.16 | 0.44 |
| MgO | 16.74 | 17.01 | 15.85 |
| Al ₂ O ₃ | 8.35 | 8.46 | 8.85 |
| SiO ₂ | 17.40 | 18.47 | 20.86 |
| P ₂ O ₅ | 0.12 | 0.14 | 0.12 |
| SO ₃ | 0.28 | 0.24 | 0.22 |
| K ₂ O | 0.15 | 0.15 | 0.14 |
| CaO | 22.20 | 21.73 | 21.95 |
| TiO ₂ | 0.38 | 0.39 | 0.44 |
| V ₂ O ₅ | 0.07 | 0.07 | 0.07 |
| Cr ₂ O ₃ | 3.75 | 4.00 | 4.22 |
| MnO | 2.19 | 2.31 | 2.49 |
| Fe ₂ O ₃ | 12.17 | 12.94 | 13.00 |
| OTH | 0.55 | 0.55 | 0.54 |

Table 3
List of composition of different AAM pastes prepared for study (in wt. %).

| Sample designation | Fraction: < 63 μm | Fraction: 63–90 μm | Fraction: 90–125 μm | Water glass (K_2SiO_3) | Water |
|--------------------|------------------------------|-------------------------------|--------------------------------|--|-------|
| 1AKS63 | 67.9 | / | / | 27.0 | 5.1 |
| 1AKS63-90 | / | 67.9 | / | 27.0 | 5.1 |
| 1AKS90-125 | / | / | 67.9 | 27.0 | 5.1 |
| 1AKS90 | 33.0 | 33.0 | / | 26.2 | 7.8 |
| 1AKS125 | 22.6 | 22.6 | 22.6 | 27.0 | 5.1 |

H_2O . The AAM pastes were manually mixed for 2 min and then placed in $20 \times 20 \times 80 \text{ mm}^3$ molds. The AAM pastes were then put in a heating chamber for three days at a temperature of 70°C to expedite the alkali-activation process and thus harden the structure. The hardened AAM were then demolded and mechanical strength measurements were recorded.

2.3. Characterization of the precursors and hardened AAM

The chemical composition of the precursors was determined using a Wavelength Dispersive X-ray Fluorescence (WD XRF) analyzer (Thermo Scientific ARL Perform X). The loss on ignition (LOI) of the precursors was determined by the standard method [39].

The reactivity of the precursors was assessed by leaching the raw materials, and was conducted by mixing 1.0 g of each fraction with 40 mL of 10 M NaOH water solution for 4 h at 22°C under continuous stirring. After filtering, the Al and Si concentrations in the liquid part were determined using an ICP-OES, Varian, model 715-ES.

Particle size distribution was measured using a CILAS 920 (Cilas, Orleans Cedex, France) particle size analyzer. Different-sized precursor powder was dispersed with microscan dispersant type C (Quantachrome Corporation, Florida, USA) during the measurements. The BET (Brunauer–Emmett–Teller) surface area of the precursors was determined using the Micromeritics ASAP 2020 equipment (N_2 adsorption at 77 K and relative pressure range of 0.05–0.3). Prior to each measurement, the precursors were heated to 70°C for 3 h and outgassed to 10–3 Torr using Micromeritics Flowprep equipment.

The mechanical strength (flexural and compressive strength) was determined after three days using Toninorm equipment (Toni Technik, Germany; force application rate of 0.05 kN/s). The flexural strength of the mix compositions was assessed under three-point bending (TPB) loading and the compressive strength was assessed under compression loading using the two broken portions from the flexural test. The reported strength measurement values represent the average results obtained from four test specimens of dimension ($20 \times 20 \times 80 \text{ mm}^3$).

XRD of the precursors and hardened AAM were determined using a PANalytical Empyrean X-ray diffractometer with $\text{CuK}\alpha$ radiation ($\lambda = 1.54 \text{ \AA}$) at a voltage of 45 kV and a current of 40 mA, in the 2θ range from 4° to 70° (scan rate = $0.026^\circ/\text{min}$). Data was then analyzed with X'Pert High Score Plus diffraction software (PANalytical), using database PDF 4 + 2015 RDB powder diffraction files. X-Ray analysis of the alumina oxide powder as a standard reference material (NIST 676a) was performed for quantitative analysis control of the multiphase mixtures and for Rietveld refinement of the powder X-ray diffractograms. Rietveld refinement was performed by X'Pert High Score Plus diffraction software with a goodness of fit of 4.9.

The pore systems of the hardened AAM were investigated by MIP using Micromeritics AutoPore IV 9500 equipment. Prior to the measurement, representative fragments of the AAM having a volume of approximately 1 cm^3 were dried in a heat chamber for 24 h at 70°C . The results of the porosimetry are defined as a function of the mercury, which penetrates porous samples under high pressure (from 0 to 318 MPa).

The different-sized precursors and time-dependent alkali-activation

reaction progress infrared spectra were recorded using FTIR with a PerkinElmer Spectrum Two spectrometer equipped with diamond/ZnSe crystal-attenuated total reflection (Universal ATR) as a solid sample support in the range from 500 to 4000 cm^{-1} . Precursors were analyzed as they were prepared for the alkali-activation process, whereas the hardened AAM were grinded prior to the analysis.

Microstructural analysis of the hardened and polished AAM cross sections was performed by a JEOL JSM-IT500 LV (back-scattered electrons image mode) SEM in a high vacuum. Quantitative analysis was performed using energy dispersive spectroscopy (EDX, Oxford instruments, using Aztec software platform). Prior SEM scanning, the samples were vacuum-dried and sputter-coated with gold.

3. Results and discussions

3.1. Characterization of precursors

To evaluate the influence of the slag particle size (after mechanical activation) on the mechanical properties (bending and compressive strength), samples of precursors of different particle sizes (fractions $d < 63$, $63 < d < 90$, $90 < d < 125 \mu\text{m}$) were first characterized using chemical composition analysis, reactivity by leaching, BET specific surface, particle size distribution, FTIR spectroscopy, and XRD determination of amorphous phase percentage.

Table 2 shows the minor differences in the chemical composition of the three different-sized fractions of slag A. The main difference was observed in the SiO_2 content, which was 20.59, 21.35, and 23.43% for fractions $d < 63 \mu\text{m}$, $63 < d < 90 \mu\text{m}$, and $90 < d < 125 \mu\text{m}$, respectively. A noticeable difference was also observed in the CaO content with values of 26.27, 25.11, and 24.66%, respectively, and the corresponding LOI was different for the three different-sized fractions.

As expected, there was an evident difference in the total specific area of the three different-sized fractions. The BET surface area of the fraction $d < 63 \mu\text{m}$ was the highest owing to the presence of the smallest particles ($7.61 \text{ m}^2/\text{g}$); for fractions $63 < d < 90 \mu\text{m}$ and $90 < d < 125 \mu\text{m}$, it was lower – 6.32 and $5.37 \text{ m}^2/\text{g}$, respectively. The particle size distribution also differed among the different precursor fractions and is presented as a cumulative value at 10, 50, and 90% (C10, C50, and C90) in Table 1.

The reactivity of the precursors, expressed as the concentration of Al and Si in the solutions of the three different-sized fractions, is presented in Table 4. It was evaluated by how extensively the precursor was affected by the attack of the alkaline solution. As expected, the precursor with the smallest particles ($d < 63 \mu\text{m}$) and consequently highest surface exhibited the highest leaching of Al and Si; 144 and 542 mg/L, respectively. These results and the BET values comply with the later mechanical strength measurements. Therefore, the precursor reactivity was greater for a higher surface area.

Using XRD, the percentage of amorphous phase was confirmed to be approximately 57% in the three fraction sizes, with no significant differences among them (Fig. 1). They primarily consisted of merwinite, calcite, chromite, and quartz (36%), with a smaller part represented by wuestite, perovskite, ankerite, corundum, periclase, dolomite, and gehlenite (7%). The varying phases in the EAF slag originate from different slag constituents, for example, the Fe phases derive from scrap iron, calcium from burnt lime, magnesium also from lime and refractory components, and the aluminum phases are formed from the

Table 4
Amount of Al and Si dissolution in relation to different-sized fractions.

| | Al [mg/L] | Si [mg/L] |
|----------------------------|-----------|-----------|
| $d < 63 \mu\text{m}$ | 144 | 542 |
| $63 < d < 90 \mu\text{m}$ | 133 | 499 |
| $90 < d < 125 \mu\text{m}$ | 126 | 414 |

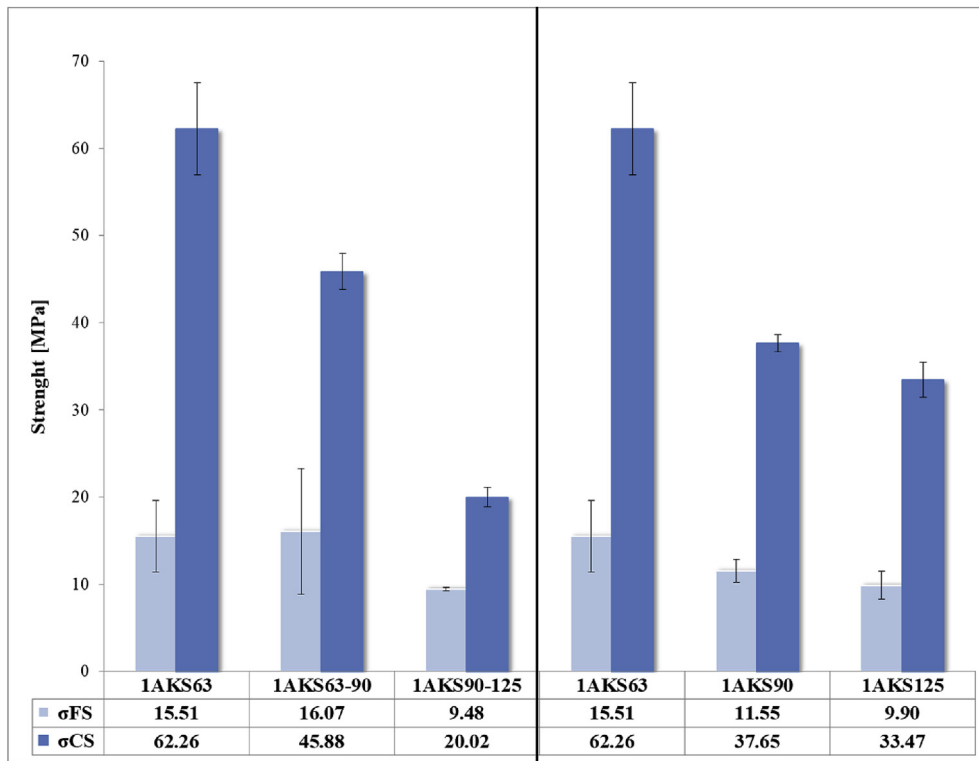


Fig. 3. Flexural (σ_{FS}) and compressive (σ_{CS}) strength measurements of AAM as function of particle size.

between the particle size and flexural strength; however, it is the lowest when the particles are the largest. Flexural strength ranges from 9.5 to 16.1 MPa, which is up to four times greater than the maximum flexural strength reported by Ozturk et al. [32].

Conversely, the compressive strength varied from 20.0 to 62.3 MPa (Fig. 3) and was significantly influenced by the particle size. In comparison, Turker et al., Peys et al., and Ozturk et al. reported the highest compressive strength values of 40.7, 16.0, and 22.0 respectively; particle size was not, however, considered an influential parameter in these

studies [32,42,43]. In contrast, Marjanović et al. studied the influence of particle size on the mechanical properties of FA-based AAM, where the particle size in specimen TENT A was comparable to the one used in this study [33]. Specimen TENT A, without mechanical activation, was comparable to our specimens using fraction size $90 < d < 125 \mu\text{m}$ (1AKS125 and 1AKS90-125). Owing to the disintegration of the prisms by hand pressure, strength measurements were not performed in the case of TENT A, whereas quite favorable results were attained in the cases of 1AKS125 and 1AKS90-125 ($\sigma_{FS} = 9.48$ and 9.90 MPa;

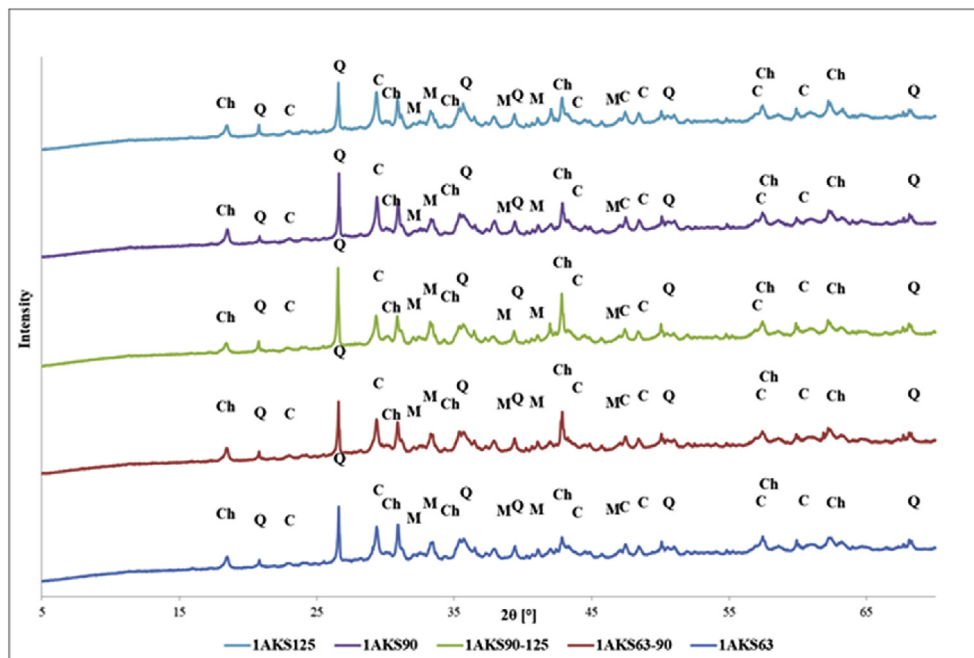


Fig. 4. X-ray diffractograms of different hardened AAM with main phases identified: Quartz (Q), Calcite (C), Chromite (Ch), and Merwinite (M).

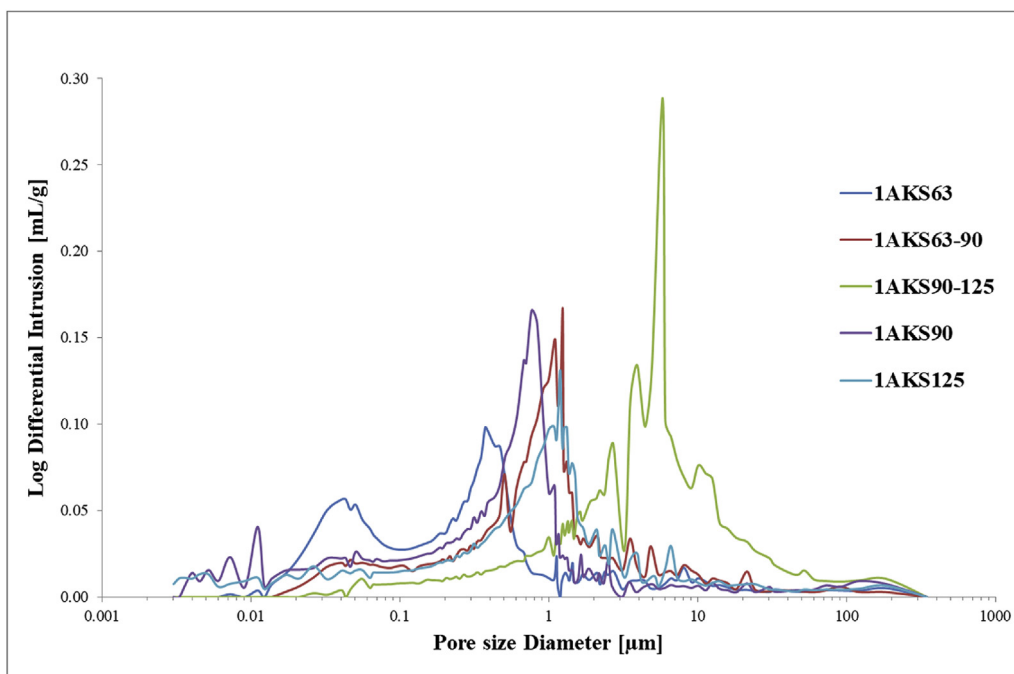


Fig. 5. Differential MIP in hardened AAM.

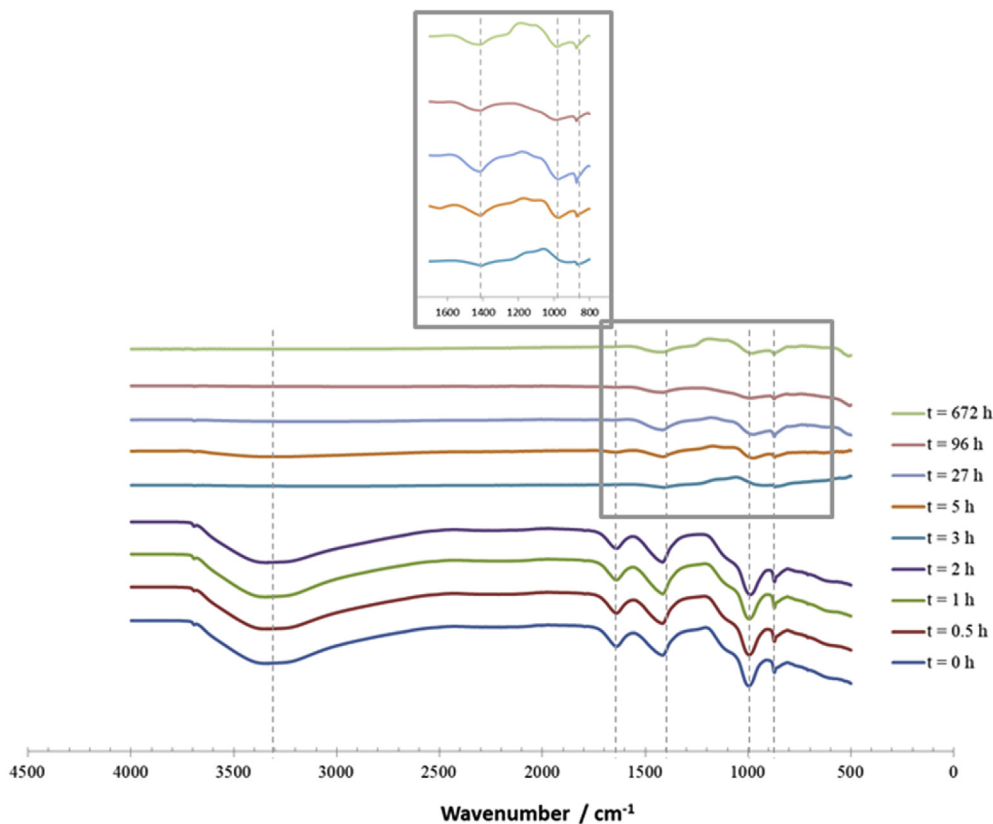


Fig. 6. Time dependent in situ infrared spectra of 1AKS90-125 mixture.

$\sigma_{CS} = 20.02$ and 33.47 MPa, respectively). However, specimen TENT A treated with 15 min of mechanical activation was comparable to our specimen 1AKS63, which demonstrated 1.1 and 2.3-times improved performance in the compressive and flexural strength measurements, respectively.

In the present study, the compressive strength increased threefold, from 20 to 62 MPa, when the particle size was halved. Furthermore,

different-sized fractions were mixed in different ratios to verify the influence of compacting on the development of mechanical strength. As observed from Fig. 3, the compressive strength was 1.7 times greater in the case of the 1AKS125 mixture, where all three fractions were added in the ratio 1:1:1 compared to the 1AKS90-125 mixture where only the fraction sized $90 < d < 125 \mu\text{m}$ was added. Conversely, the mixture 1AKS90 did not support this trend, and the compressive strength

Table 5
Differential MIP data.

| | 1AKS63 | 1AKS63-90 | 1AKS90-125 | 1AKS90 | 1AKS125 |
|-------------------------------------|--------|-----------|------------|--------|---------|
| Total pore area [m ² /g] | 3.85 | 1.50 | 0.53 | 7.16 | 6.19 |
| Porosity [%] | 20.00 | 20.93 | 26.27 | 22.44 | 21.13 |
| Median Pore Diameter (Volume) [μm] | 0.29 | 0.92 | 5.12 | 0.56 | 0.89 |
| Median Pore Diameter (Area) [μm] | 0.04 | 0.06 | 0.11 | 0.01 | 0.01 |
| Average Pore Diameter (4V/A) [μm] | 0.09 | 0.26 | 0.97 | 0.06 | 0.06 |
| Apparent (skeletal) Density [g/mL] | 2.73 | 2.73 | 2.76 | 2.73 | 2.77 |

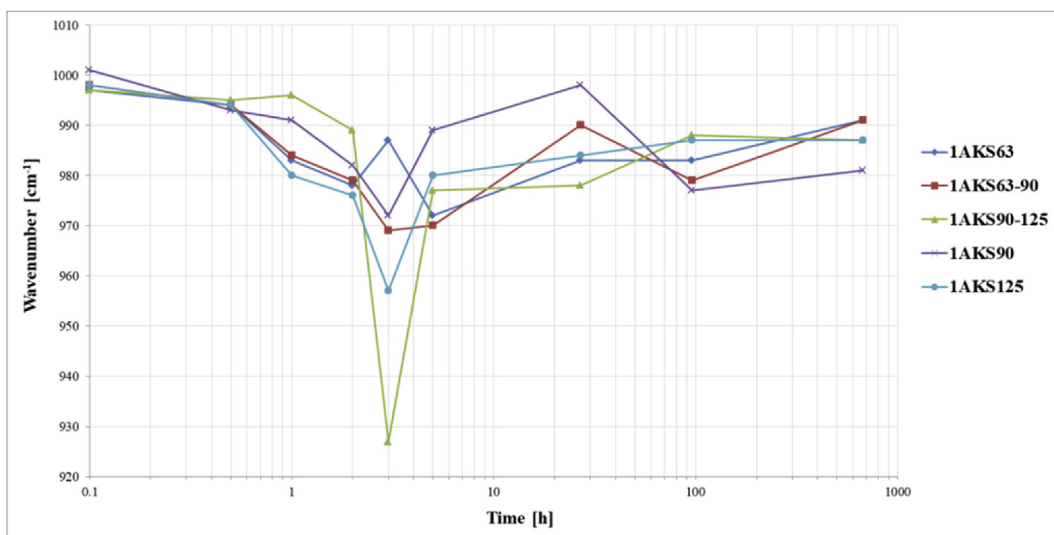


Fig. 7. Si-O-T band shifts of different AAM pastes.

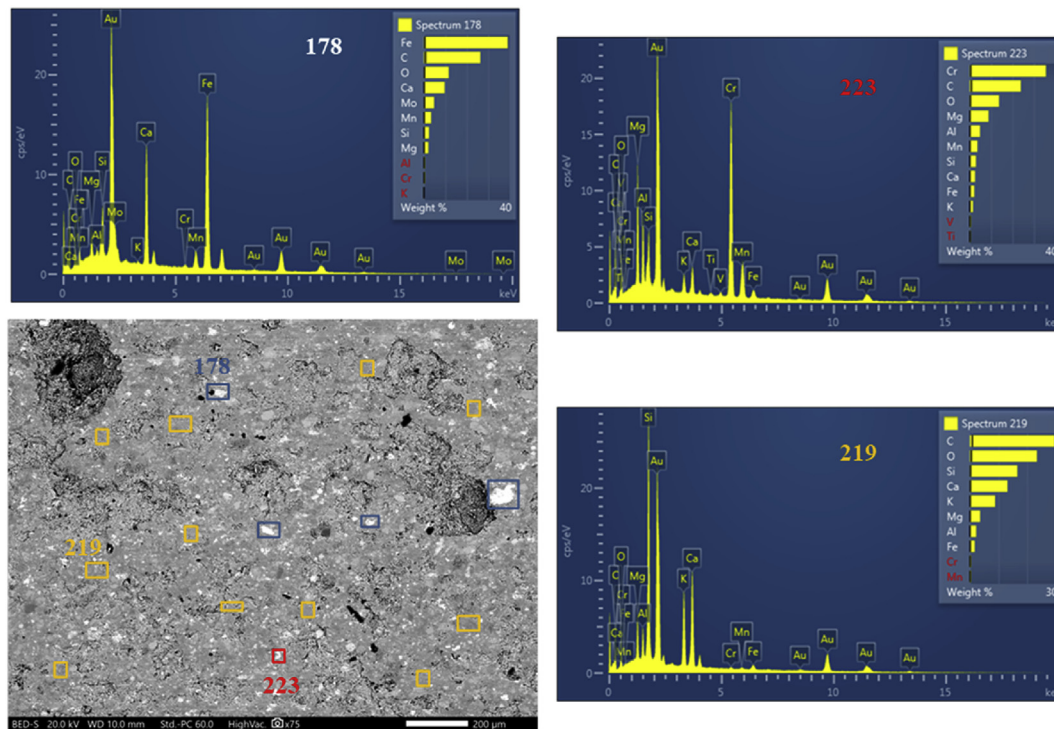


Fig. 8. SEM and EDS analysis of 1AKS63 sample.

actually decreased by 20% compared to mixture 1AKS63-90; this can be partially ascribed to the lower porosity of the latter (see Fig. 5).

3.3. Mineralogical and microstructural analysis of AAM

X-ray powder diffraction patterns of hardened AAM reveal that there were no significant differences among them in terms of

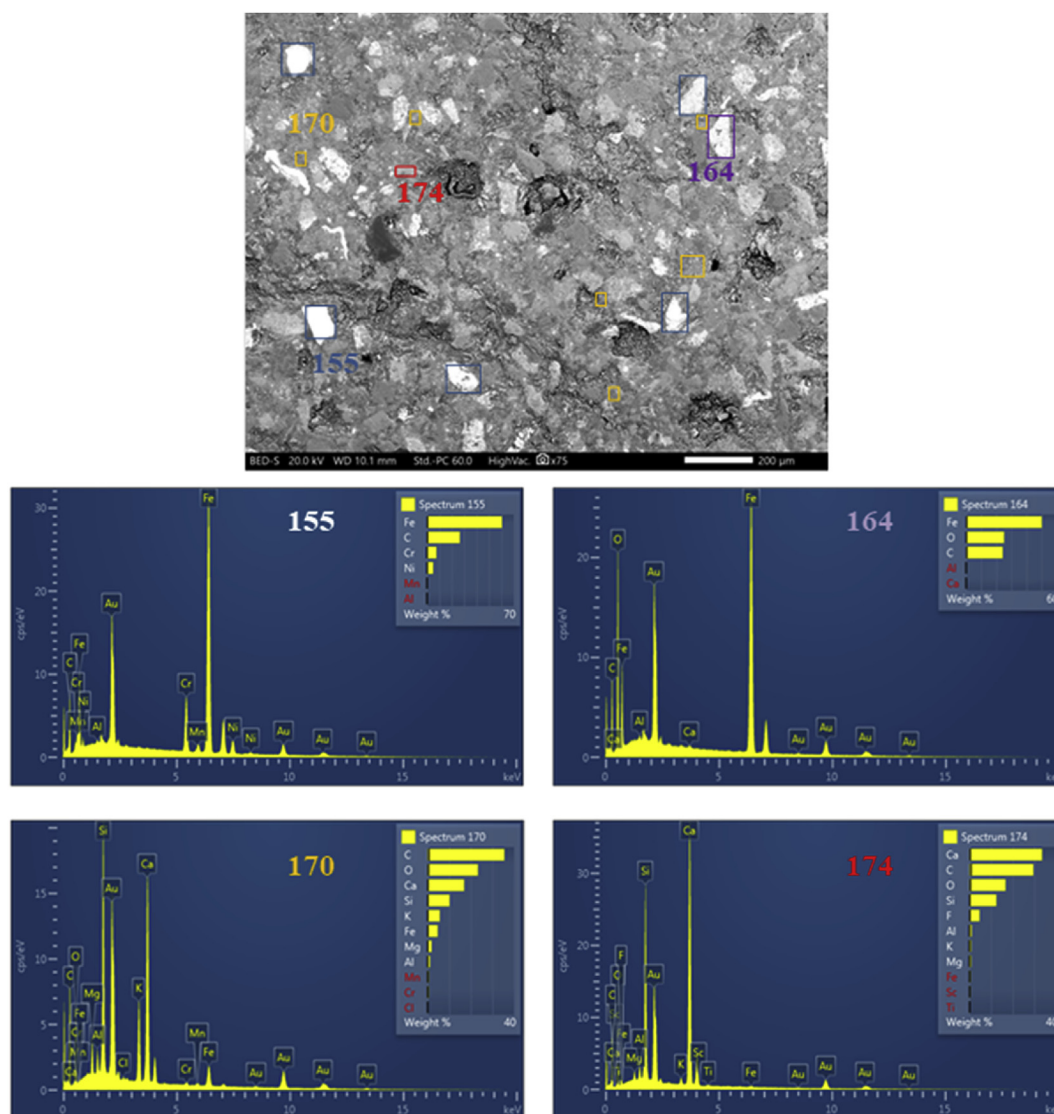


Fig. 9. SEM and EDS analysis of 1AKS90-125 sample.

mineralogical composition (Fig. 4). The percentage of the glassy phase increased to approximately 61% because of the addition of the activator, which had an amorphous nature. The crystalline content did not change significantly compared to the precursor mineralogical composition, as was also observed by Marjanović et al. [33].

The pore structure of AAM has a significant influence on its performance. Microstructural evaluation using MIP was therefore performed; this confirmed that porosity was the lowest in AAM with the smallest particle size (1AKS63). This mixture was also the only one demonstrating a bimodal distribution of pores (Fig. 5), with two intrusion peaks at approximately 0.04 μm and 0.4 μm . As the particle size increased, the porosity also increased, and the intrusion peaks moved towards larger pores, ranging from 0.7 to 5.8 μm . Interestingly, the highest pore area was achieved in 1AKS90, where two slag fractions were used as precursors (Table 5). Herein, the trend associating a reduced porosity with greater mechanical strength was confirmed. Sedira et al. observed the reverse trend; however, the chemical composition among the tested specimens was not equal [44]. The specimen with comparable porosity (RB03TM07, 25.98%), did demonstrate superior performance compared to 1AKS90-125 (26.27%), the compressive strength being 39 and 20 MPa, respectively [44]. Apparently, the porosity in this case was not the dominant factor influencing the mechanical strength; rather, this could be partially ascribed to a smaller

average pore diameter, which was 0.02 and 0.97 μm for RB03TM07 and 1AKS90-125, respectively. However, the main difference, which most probably influenced the compressive strength, was a lower liquid to solid ratio (L/S) in the case of the RB03TM07 specimen (0.25 and 0.47 for RB03TM07 and 1AKS90-125, respectively).

The time-dependent microstructural changes during the alkali-activation process were monitored using in situ infrared spectroscopy for $t = 0, 0.5, 1, 2, 3, 5, 27, 96,$ and 672 h (Fig. 6). Compared to the IR spectra of the precursors, additional bands present at $t = 0$ were attributed to the symmetric O–H stretching and H–O–H bending vibrations (at approximately 3300 and 1650 cm^{-1} , respectively). Over the alkali-activation process time, the intensity of these bands decreased owing to water consumption in the reaction, forming hardened AAM [7,38]. The band at approximately 1000 cm^{-1} assigned to the Si–O–T vibration experienced major changes during the alkali-activation process, as the band shifted around this value. As can be observed from Fig. 7, there is first a minor drop in the peak position, followed by a major difference in wavenumber values 3 h after the process initiation; this suggests when the greatest difference in the alkali-activation process affected by the particle size as an influential parameter occurs. Interestingly, for the mixture with the smallest particle size (1AKS63), the value marginally increases (987 cm^{-1}), whereas for mixtures with the largest particle sizes (1AKS125 and 1AKS90-125), the decrease in

wavenumber values is the most distinct (957 and 927 cm^{-1} , respectively). These findings are in compliance with previously reported facts that a rapid set of geopolymerization in the first two to 5 h occurs, resulting in a significant percentage increase of total compressive strength [45]. A similar trend was observed by Rovnanik et al., where the effect of different curing temperatures (10, 20, and 80 °C) on a geopolymerization reaction in metakaolin-based geopolymers was monitored with infrared spectroscopy [24]. In that case, the highest drop in wavenumber value was observed in the specimen cured at the highest temperature (i. e. 80 °C), which also exhibited the highest mechanical strength at that time. In our case, the influence of the porosity, which is the highest in the case of the 1AKR90-125 specimen, was the prevailing factor influencing the mechanical properties. Moreover, because the potassium silicate and water addition, and curing regime are the same for all mixtures, and furthermore, the infrared spectra of the different fractions of the precursors were the same (Fig. 2), the difference in wavelength values can only occur as a consequence of the diverse reactivity of the different-sized precursors, which was also confirmed by a leaching test (Table 4). After 96 h of the alkali-activation process, the differences in the wavenumber values were again minimal.

The images from the SEM and Energy Dispersive X-ray Spectroscopy (EDS) analysis of the selected polished surfaces of the hardened AAM samples presented in Figs. 8 and 9 reveal the main differences among the mixtures. When comparing two extremes at the same magnification (specimens 1AKS63 and 1AKS90-125 in Figs. 8 and 9, respectively), it is observed that the particles are noticeably larger in the AAM matrix with 125 μm -sized particles, and the activation/reaction process appears to be incomplete. The chemical composition of the unreacted particles supports the XRD analysis because Cr and Fe from Chromite, Fe from Wuestite, and Ca from Calcite (in Fig. 8, spectra 178 and 223, and in Fig. 9, spectra 155 and 164) present the most abundant unreacted particles. Because these particles did not react with the alkali, they represent only the filling in AAM. A similar form has also been observed by other researchers. For example, Burciaga-Diaz et al. noted unreacted GBF slag particles in the AAM specimen after 28 days of curing. Interestingly, after 720 days, the number of unreacted GBF slag particles decreased owing to the advancement of the hydration reactions [30]. Conversely, in an AAM matrix with particle size less than 63 μm , the grains are barely noticeable. The matrix/gel formed during the alkali-activation process is encircled in orange in both figures with spectra 219 and 170 representing the most commonly observed gel composition. It can be noticed that the wt. % of Si is greater in the case of the 1AKR63 specimen owing to the higher reactivity of the smaller grains. In all cases, Ca is present in the gel matrix.

4. Conclusions

This study investigates the suitability of milled and sieved EAF slag from a Slovenian factory as a precursor in an alkali-activation process. Five different AAM pastes with different particle sizes were studied to evaluate the influence of particle size on the mechanical properties, and their mineralogical, microstructural, and chemical makeup. Chemical analysis indicated only marginal differences among the input materials that consisted of different-sized fractions, whereas BET specific surface area and reactivity of the precursors differed significantly – the finest particles with the largest surface area having higher reactivity contributing to higher mechanical strength. However, the mineralogical differences between the precursors and hardened AAM were negligible. The results of the strength measurements revealed that particle size did not have a specific influence on flexural strength, yet it had a significant influence on the compressive strength, i.e., a threefold increase when the particle size was halved. Microstructural evaluation using MIP confirmed that porosity is the least in AAM with the smallest particle size (1AKS63). In situ infrared spectroscopy revealed that the greatest difference due to the particle size in the alkali-activation process occurred 3 h after process initiation, where a major difference in

wavenumber values was observed. Microstructural analysis using SEM revealed differences in mixtures, whereas differences in input particle size were also observed in the AAM, i.e., in an AAM matrix with particles of size 125 μm , the particles are noticeably larger and the activation appeared to be incomplete. Based on our results, we conclude that particle size manipulation can significantly influence the mechanical properties of AAM.

Acknowledgements

This work has been financed under the project FLOW: Lightweight alkali activated composite foams based on secondary raw materials, Project ID-94, 2017 ERA-MIN 2 Joint Call.

References

- [1] R.M. Andrew, Global CO₂ emissions from cement production, *Earth Syst. Sci. Data* 10 (2018) 195–217 <https://doi.org/10.5194/essd-10-195-2018>.
- [2] J.L. Provis, J.S.J. van Deventer (Eds.), *Alkali Activated Materials: State-Of-The-Art Report*, RILEM TC 224-AAM, Springer/RILEM, Berlin, 2013.
- [3] M. Clausi, S.C. Tarantino, L.L. Magnani, M.P. Riccardi, C. Tedeschi, M. Zema, Metakaolin as a precursor of materials for applications in Cultural Heritage: geopolymer-based mortars with ornamental stone aggregates, *Appl. Clay Sci.* 132 (2016) 589–599 <https://doi.org/10.1016/j.clay.2016.08.009>.
- [4] I. Balczar, T. Korim, A. Kovacs, E. Mako, Mechanochemical and thermal activation of kaolin for manufacturing geopolymer mortars - comparative study, *Ceram. Int.* 42 (2016) 15367–15375 <https://doi.org/10.1016/j.ceramint.2016.06.182>.
- [5] W. Rakngan, T. Williamson, R.D. Ferron, G. Sant, M.C.G. Juenger, Controlling workability in alkali-activated Class C fly ash, *Constr. Build. Mater.* 183 (2018) 226–233 <https://doi.org/10.1016/j.conbuildmat.2018.06.174>.
- [6] J.N.Y. Djobo, A. Elimbi, H.K. Tchakoute, S. Kumar, Mechanical properties and durability of volcanic ash based geopolymer mortars, *Constr. Build. Mater.* 124 (2016) 606–614 <https://doi.org/10.1016/j.conbuildmat.2016.07.141>.
- [7] E. Adesanya, K. Ohenoja, P. Kinnunen, M. Illikainen, Alkali activation of ladle slag from steel-making process, *J. Sustain. Metall.* 3 (2017) 300–310 <https://doi.org/10.1007/s40831-016-0089-x>.
- [8] D.L.Y. Kong, J.G. Sanjayan, Effect of elevated temperatures on geopolymer paste, mortar and concrete, *Cement Concr. Res.* 40 (2010) 334–339 <https://doi.org/10.1016/j.cemconres.2009.10.017>.
- [9] K. Sagoe-Crentsil, T. Brown, A. Taylor, Drying shrinkage and creep performance of geopolymer concrete, *J. Sustain. Cement-Based Mater.* 2 (2013) 35–42 <https://doi.org/10.1080/21650373.2013.764963>.
- [10] T.A. Aiken, W. Sha, J. Kwasny, M.N. Soutsos, Resistance of geopolymer and Portland cement based systems to silage effluent attack, *Cement Concr. Res.* 92 (2017) 56–65 <https://doi.org/10.1016/j.cemconres.2016.11.015>.
- [11] T. Bakharev, Resistance of geopolymer mortars to acid attack, *Cement Concr. Res.* 35 (2005) 658–670 <https://doi.org/10.1016/j.cemconres.2004.06.005>.
- [12] A.M.-M. Al Bakri, H. Kamarudin, M. Binhussain, I.K. Nizar, A.R. Rafiza, Y. Zarina, Comparison of geopolymer fly ash and ordinary portland cement to the strength of concrete, *Adv. Sci. Lett.* 19 (2013) 3592–3595 <https://doi.org/10.1166/asl.2013.5187>.
- [13] J.L. Provis, Alkali-activated materials, *Cement Concr. Res.* 114 (2018) 40–48 <https://doi.org/10.1016/j.cemconres.2017.02.009>.
- [14] B.V. DSTU, 2.7-181, *Alkaline Cements Specifications*, National Standard of Ukraine, Kiev, 2009.
- [15] H.M. Khater, H.A.A. el Gawaad, Characterization of alkali activated geopolymer mortar doped with MWCNT, *Constr. Build. Mater.* 102 (2016) 329–337 <https://doi.org/10.1016/j.conbuildmat.2015.10.121>.
- [16] T. Bakharev, J.G. Sanjayan, Y.B. Cheng, Alkali activation of Australian slag cements, *Cement Concr. Res.* 29 (1999) 113–120 [https://doi.org/10.1016/s0008-8846\(98\)00170-7](https://doi.org/10.1016/s0008-8846(98)00170-7).
- [17] T.-H. Lu, Y.-L. Chen, P.-H. Shih, J.-E. Chang, Use of basic oxygen furnace slag fines in the production of cementitious mortars and the effects on mortar expansion, *Constr. Build. Mater.* 167 (2018) 768–774 <https://doi.org/10.1016/j.conbuildmat.2018.02.102>.
- [18] L. Coppola, A. Buoso, D. Coffetti, P. Kara, S. Lorenzi, Electric arc furnace granulated slag for sustainable concrete, *Constr. Build. Mater.* 123 (2016) 115–119 <https://doi.org/10.1016/j.conbuildmat.2016.06.142>.
- [19] I. Santamaria-Vicario, A. Rodriguez, C. Junco, S. Gutierrez-Gonzalez, V. Calderon, Durability behavior of steelmaking slag masonry mortars, *Mater. Des.* 97 (2016) 307–315 <https://doi.org/10.1016/j.matdes.2016.02.080>.
- [20] N.H. Roslan, M. Ismail, Z. Abdul-Majid, S. Ghoreishiamiri, B. Muhammad, Performance of steel slag and steel sludge in concrete, *Constr. Build. Mater.* 104 (2016) 16–24 <https://doi.org/10.1016/j.conbuildmat.2015.12.008>.
- [21] E. Adesanya, K. Ohenoja, P. Kinnunen, M. Illikainen, Properties and durability of alkali-activated ladle slag, *Mater. Struct.* 50 (50) (2017) 255 <https://doi.org/10.1617/s11527-017-1125-4>.
- [22] W.-T. Kuo, T.-C. Hou, Engineering properties of alkali-activated binders by use of desulfurization slag and GGBFS, *Constr. Build. Mater.* 66 (2014) 229–234 <https://doi.org/10.1016/j.conbuildmat.2014.05.056>.
- [23] EUROSLAG, The European Association representing metallurgical slag producers

- and processors, <http://www.euroslag.com>, Accessed date: 22 July 2019.
- [24] P. Rovnanik, Effect of curing temperature on the development of hard structure of metakaolin-based geopolymer, *Constr. Build. Mater.* 24 (2010) 1176–1183 <https://doi.org/10.1016/j.conbuildmat.2009.12.023>.
- [25] N. Marjanović, M. Komljenović, Z. Baščarević, V. Nikolić, R. Petrović, Physical-mechanical and microstructural properties of alkali-activated fly ash-blast furnace slag blends, *Ceram. Int.* 41 (2015) 1421–1435 <https://doi.org/10.1016/j.ceramint.2014.09.075>.
- [26] P. Duxson, J.L. Provis, G.C. Lukey, S.W. Mallicoat, W.M. Kriven, J.S.J. van Deventer, Understanding the relationship between geopolymer composition, microstructure and mechanical properties, *Colloids Surf., A* 269 (2005) 47–58 <https://doi.org/10.1016/j.colsurfa.2005.06.060>.
- [27] M.L. Granizo, M.T. Blanco-Varela, S. Martinez-Ramirez, Alkali activation of metakaolins: parameters affecting mechanical, structural and microstructural properties, *J. Mater. Sci.* 42 (2007) 2934–2943 <https://doi.org/10.1007/s10853-006-0565-y>.
- [28] E. Kamseu, M. Cannio, E.A. Obonyo, F. Tobias, M.C. Bignozzi, V.M. Sglavo, C. Leonelli, Metakaolin-based inorganic polymer composite: effects of fine aggregate composition and structure on porosity evolution, microstructure and mechanical properties, *Cement Concr. Compos.* 53 (2014) 258–269 <https://doi.org/10.1016/j.cemconcomp.2014.07.008>.
- [29] S.D. Wang, K.L. Scrivener, P.L. Pratt, Factors affecting the strength of alkali-activated slag, *Cement Concr. Res.* 24 (1994) 1033–1043 [https://doi.org/10.1016/0008-8846\(94\)90026-4](https://doi.org/10.1016/0008-8846(94)90026-4).
- [30] O. Burciaga-Diaz, J.I. Escalante-Garcia, Structure, mechanisms of reaction, and strength of an alkali-activated blast-furnace slag, *J. Am. Ceram. Soc.* 96 (2013) 3939–3948 <https://doi.org/10.1111/jace.12620>.
- [31] B.S. Gebregziabihier, R. Thomas, S. Peethamparan, Very early-age reaction kinetics and microstructural development in alkali-activated slag, *Cement Concr. Compos.* 55 (2015) 91–102 <https://doi.org/10.1016/j.cemconcomp.2014.09.001>.
- [32] M. Ozturk, M.B. Bankir, O.S. Bolukbasi, U.K. Sevim, Alkali activation of electric arc furnace slag: mechanical properties and micro analyzes, *J. Build. Eng.* 21 (2019) 97–105 <https://doi.org/10.1016/j.jobbe.2018.10.005>.
- [33] N. Marjanović, M. Komljenović, Z. Bascarević, V. Nikolić, Improving reactivity of fly ash and properties of ensuing geopolymers through mechanical activation, *Constr. Build. Mater.* 57 (2014) 151–162 <https://doi.org/10.1016/j.conbuildmat.2014.01.095>.
- [34] B. Khaydarov, D. Suvorov, A. Pazniak, E. Kolesnikov, V. Gorchakov, S. Mamulat, D. Kuznetsov, Efficient method of producing clinker-free binding materials using electromagnetic vortex milling, *Mater. Lett.* 226 (2018) 13–18 <https://doi.org/10.1016/j.matlet.2018.05.016>.
- [35] H.A. Abdel-Gawwad, S.R.V. Garcia, H.S. Hassan, Thermal activation of air cooled slag to create one-part alkali activated cement, *Ceram. Int.* 44 (2018) 14935–14939 <https://doi.org/10.1016/j.ceramint.2018.05.089>.
- [36] A.D. Hounsi, G.L. Lecomte-Nana, G. Djeteli, P. Blanchart, Kaolin-based geopolymers: effect of mechanical activation and curing process, *Constr. Build. Mater.* 42 (2013) 105–113 <https://doi.org/10.1016/j.conbuildmat.2012.12.069>.
- [37] E. Furlani, S. Maschio, M. Magnan, E. Aneggi, F. Andreatta, M. Lekka, A. Lanzutti, L. Fedrizzi, Synthesis and characterization of geopolymers containing blends of unprocessed steel slag and metakaolin: the role of slag particle size, *Ceram. Int.* 44 (2018) 5226–5232 <https://doi.org/10.1016/j.ceramint.2017.12.131>.
- [38] M. Češnovar, K. Traven, B. Horvat, V. Ducman, The potential of ladle slag and Electric Arc furnace slag use in synthesizing alkali activated materials; the influence of curing on mechanical properties, *Materials* 12 (2019) 1173 <https://doi.org/10.3390/ma12071173>.
- [39] EN 196-2 – Method of Testing Cement – Part 2, *Chemical Analysis of Cement*, 2013.
- [40] K. Komnitsas, D. Zaharaki, A. Vlachou, G. Bartzas, M. Galetakis, Effect of synthesis parameters on the quality of construction and demolition wastes (CDW) geopolymers, *Adv. Powder Technol.* 26 (2015) 368–376 <https://doi.org/10.1016/j.apt.2014.11.012>.
- [41] X. Gao, Q.L. Yu, H.J.H. Brouwers, Reaction kinetics, gel character and strength of ambient temperature cured alkali activated slag-fly ash blends, *Constr. Build. Mater.* 80 (2015) 105–115 <https://doi.org/10.1016/j.conbuildmat.2015.01.065>.
- [42] H.T. Turker, M. Balcikanli, I.H. Durmus, E. Ozbay, M. Erdemir, Microstructural alteration of alkali activated slag mortars depend on exposed high temperature level, *Constr. Build. Mater.* 104 (2016) 169–180 <https://doi.org/10.1016/j.conbuildmat.2015.12.070>.
- [43] A. Peys, L. Arnout, B. Blanpain, H. Rahier, K. van Acker, Y. Pontikes, Mix-design parameters and real-life considerations in the pursuit of lower environmental impact inorganic polymers, *Waste Biomass Valori* 9 (2018) 879–889 <https://doi.org/10.1007/s12649-017-9877-1>.
- [44] N. Sedira, J. Castro-Gomes, M. Magrinho, Red clay brick and tungsten mining waste-based alkali-activated binder: microstructural and mechanical properties, *Constr. Build. Mater.* 190 (2018) 1034–1048 <https://doi.org/10.1016/j.conbuildmat.2018.09.153>.
- [45] D. Khale, R. Chaudhary, Mechanism of geopolymerization and factors influencing its development: a review, *J. Mater. Sci.* 42 (2007) 729–746 <https://doi.org/10.1007/s10853-006-0401-4>.